Characterization of Acquisition Geometry of Pinhole SPECT

Dirk Bequé*, *Student Member, IEEE*, Johan Nuyts, *Member, IEEE*, Guy Bormans, Paul Suetens, *Member, IEEE*, and Patrick Dupont

***Abstract*— A method is presented to estimate the acquisition geometry of a pinhole SPECT camera with a circular detector orbit. This information is needed for the reconstruction of tomographic images. The calibration uses the point source projection locations of a tomographic acquisition of three point sources located at known distances from each other. It is shown that this simple phantom provides the necessary and sufficient information for the proposed calibration method. The knowledge of two of the distances between the point sources proves to be essential. The geometry is estimated by fitting analytically calculated projections to the measured ones, using a simple least squares Powell-algorithm. Some mild a priori knowledge is used to constrain the solutions of the fit. Several of the geometrical parameters are however highly correlated. The effect of these correlations on the reconstructed images is evaluated in simulation studies and related to the estimation accuracy. The highly correlated detector tilt and electrical shift are shown to be the critical parameters for accurate image reconstruction. The performance of the algorithm is finally demonstrated by phantom measurements. The method is based on a single SPECT-scan of a simple calibration phantom, executed immediately after the actual SPECT acquisition. The method is also applicable to cone-beam SPECT and X-ray CT.**

***Index Terms*—Pinhole, geometric calibration, acquisition geometry, SPECT.**

I. Introduction

Because of their converging beam geometry, pinhole cameras can provide high resolution images of targets close to the focal point. The pinhole image magnification allows a spatial resolution of projections and reconstructed images (pinhole SPECT) below the intrinsic resolution of the γ-camera. This superior resolution in comparison with parallel hole imaging, comes at the expense of a severely reduced field of view. This limited field of view restricts the clinical use of pinhole SPECT to specific, smaller parts of the human body. Nevertheless, some potential clinical applications, like for example thyroid scans, have been reported in literature [1–5]. Further, the small field of view poses no problem for imaging small laboratory animals, like mice and rats. Such imaging also requires a high spatial resolution. Therefore, pinhole SPECT provides an appropriate imaging technique for small animal studies [6]. These studies are a powerful tool for studying animal models of human disease or new radiopharmaceuticals. In recent years several studies using pinhole SPECT have been reported in literature [7–14], with up to submillimeter spatial resolution [7, 13].

To avoid artifacts and loss of resolution, the reconstruction of data acquired with a pinhole camera requires a detailed description of the camera geometry [15–22]. For cameras with the detector rotating on a circular orbit around the rotation axis, seven parameters are necessary and sufficient to completely describe this acquisition geometry [18,21]. The focal length f and the electrical shifts e_u and e_v constitute the intrinsic pinhole parameters. Their value is independent of the position of the detector. The focal length is the distance between the focal point and the detector and the electrical shifts describe a collective translation of the projection images, caused by drift of the detector hardware. Regional distortions in the projection images are not taken into account. The extrinsic parameters d, m, Φ and Ψ depend on the position of the detector with respect to the axis of rotation. They are conveniently described by use of the central ray : the pinhole projection ray orthogonal to the detector. The mechanical offset m is the offset of this central ray from the rotation axis. The distance d is the distance along the central ray between the focal point and the rotation axis, in absence of the mechanical offset m. It determines the radius of the circular orbit of the detector. The tilt Φ is the angle between the detector and the axis of rotation, or equivalently the complement of the angle between the central ray and the axis of rotation. Finally, the twist Ψ describes the orientation of the detector pixel grid as a rotation around an axis parallel to the central ray. All parameters are assumed to remain constant during the pinhole acquisition. Figure 1, 2 and 3 illustrate the above parameters and table I summarizes them.

The extrinsic parameters depend on the position of the detector and the electrical shifts may vary in time. Also remounting the same collimator has been reported to cause changes of the mechanical offset [16]. Since these geomet-

This work was supported by grant OT-00/32 of K.U.Leuven and by grant G.0174.03 of FWO.

*D. Bequé, J. Nuyts and P. Dupont are with the Department of Nuclear Medicine, University Hospital Gasthuisberg, B-3000 Leuven, Belgium (e-mail: Dirk.Beque@uz.kuleuven.ac.be). P. Dupont is post-doctoral researcher of the Flemish Fund for Scientific Research (FWO).

G. Bormans is with the Laboratory for Radiopharmaceutical Chemistry, University Hospital Gasthuisberg, B-3000 Leuven, Belgium.

P. Suetens is with the Laboratory for Medical Image Computing, Radiology-ESAT/PSI, University Hospital Gasthuisberg, B-3000 Leuven, Belgium.

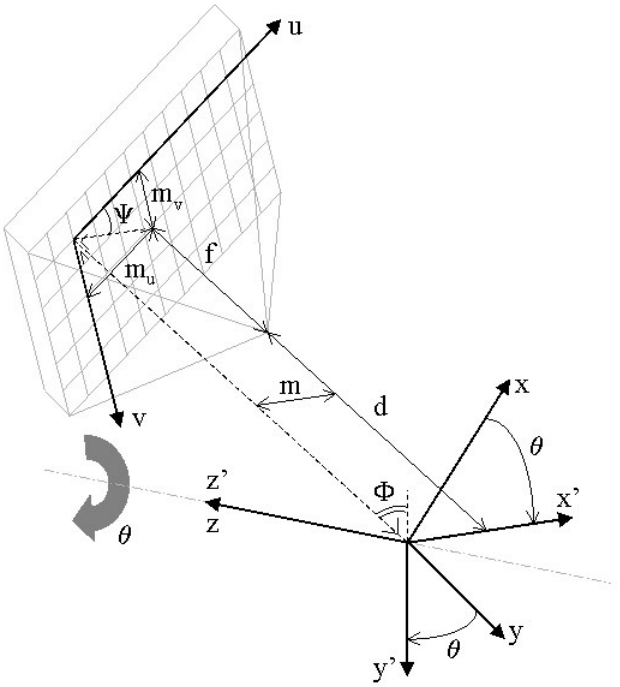

Fig. 1. Camera-Image Geometry: the z-axis is the rotation axis of the imaging system and the xyz-origin is located to make the central ray intersect the x'-axis.

TABLE I
PINHOLE PARAMETERS.

Symbol	Name	Type	Figure
f	Focal length	Intrinsic	1,3
d	Distance d	Extrinsic	1,3
m	Mechanical offset	Extrinsic	1,3
e_u	Electrical shift	Intrinsic	2
e_v			
Φ	Tilt	Extrinsic	1,2
Ψ	Twist	Extrinsic	1,2

rical changes call for frequent calibration of the pinhole camera, we aim for an easy calibration procedure that allows the determination of all seven geometrical parameters from a single calibration measurement. The idea is to perform a calibration immediately after each (series of) acquisition(s), with the camera left in the acquisition geometry. The object in the field of view is simply replaced by a calibration phantom and a second (possibly shorter) acquisition is performed. The phantom used for calibration must be simple and easy to position under the camera. In addition, the simplicity of the phantom design should make it equally suited for cone beam SPECT and X-ray CT, which encounter similar calibration problems.

Several methods have already been proposed to calculate or estimate the geometry of a pinhole camera, cone beam camera or X-ray CT. First Gullberg *et al.* [15] proposed a very straightforward approach by fitting the calculated projections of a point source to the measured ones by a least squares minimization. The method assumes an ideal camera geometry, except for the electrical shift. The method was later extended to include the mechanical offset [16] and for the calibration of astigmatic collimators [17]. The method has the advantage of using a very simple calibration phantom, applicable for SPECT as well as CT. Some calibration parameters prove however to be highly correlated and local minima in the minimization cost function are expected to exist [15–18, 21]. This reduces the accuracy of the parameter estimates and makes them dependent on the initial estimates of the fitting procedure. To avoid this, Li *et al.* [16] and Wang *et al.* [17] incorporated a priori knowledge to confine the solutions to a region near the global minimum of the cost function.

Rizo *et al.* [18] take a different approach by performing a series of measurements to avoid the correlations in the simultaneous estimation of all parameters. The geometrical parameters are separated into the intrinsic and extrinsic parameters. The intrinsic parameters are measured using a grid of point sources, carefully placed with respect to the detector. The phantom is specifically designed to fit on the cone beam collimator. The extrinsic parameters are again estimated by non-linear fitting using the tomographic projection data of a single point source. The method estimates all seven geometrical parameters and also allows to measure the size of the detector pixels. Kyriakopoulos *et al.* [19] adopt the idea of separate measurements for the intrinsic and extrinsic parameters. The intrinsic parameters are measured in a similar way as in the method of Rizo *et al.*. The extrinsic parameters are estimated by nonlinear fitting, using the projection of a regular grid of point sources. The calibration is performed for every projection angle, so the detector rotation is not restricted to a circular orbit. The range of the projection angle is however limited.

Finally, Bronnikov *et al.* [20] and Noo *et al.* [21, 22] use algebraic approaches to avoid the difficult non-linear estimation problems of the above methods. Bronnikov *et al.* make strong assumptions about the camera geometry, but need only two 180 degree opposed projections to calculate it. Noo *et al.* calculate the complete camera geometry, except for the detector tilt, using the tomographic projection data of two point sources at a known distance from each other. The parameters are calculated from the mathematical description of the ellipses that the point source projections describe in the projection images during the acquisition.

Because of the parameter correlations, complex and system dependent calibration phantoms or multiple calibration measurements seem necessary for the accurate calculation of a complete pinhole geometry. Even small errors on one of the parameter estimates can cause visibly detrimental effects in the reconstructed image [21]. The question remains however whether this also applies for correlated errors. We propose a new calibration method to estimate all seven parameters with a single calibration measurement using non-linear fitting. The method is based on the tomographic projection data of three point sources at known distances from each other. The method incor-

porates some a priori knowledge, mainly to avoid local minima of the cost function. Its performance is not evaluated for the accuracy of the parameter estimates, but for image reconstruction accuracy. This approach tolerates correlated errors, as long as they do not influence the reconstructed image significantly.

Section II provides the theoretical framework of the proposed calibration method. Subsections A and B describe the geometry of a pinhole camera and its projection of a point source. Subsection C treats the estimation of the pinhole geometry from point source projections. It determines the necessary number of point sources and the conditions on their locations in the field of view. Subsection D finally illustrates how the fitting procedure is used to calibrate the camera and how to incorporate a priori knowledge. Section III presents the simulations and experiments performed to evaluate the methods performance. First the necessary number of point sources is studied in subsection A. Further, in section III B, the accuracy of the estimated camera geometry is determined. The implications of the estimation errors on the accuracy of reconstruction are assessed in subsection C. Section III D finally evaluates the performance of the method by real calibration measurements. The results of the above experiments are presented in section IV and discussed in section V.

II. Theory

A. Camera-Image Geometry

Consider a pinhole system consisting of a flat detector and a pinhole collimator with an infinitely small aperture. The detector rotates on a circular orbit during acquisition. The 3D spatial activity distribution $A(x, y, z)$ is projected through the pinhole focus onto the detector. The distribution is defined in the right handed Cartesian coordinate system xyz, with the z-axis along the rotation axis. The projection $P_\theta(u, v)$, for the detector at position θ on the circular orbit, is defined in the uv Cartesian coordinate system. These axes are fixed to the detector along known directions in the detector element grid. The origin of the uv coordinate system is the perpendicular projection of the origin of the xyz system on the detector, as shown in figure 1. The rotation angle θ is defined as the angle between the detector surface and the x-axis, measured in the xy-plane.

At every detector position θ, the relative orientation of the activity distribution and the detector is different. By correcting for this rotation θ, the same distribution can be expressed in a new coordinate system $x'y'z'$ rotating with the uv-system around its own z'-axis, keeping the x'-axis parallel to the detector surface.

$$\begin{bmatrix} x' \\ y' \\ z' \end{bmatrix} = \begin{bmatrix} cos\theta & sin\theta & 0 \\ -sin\theta & cos\theta & 0 \\ 0 & 0 & 1 \end{bmatrix} \begin{bmatrix} x \\ y \\ z \end{bmatrix} \qquad (1)$$

Notice that the angle θ expresses the relative orientation of the detector and the image $A(x, y, z)$ with respect to each other. Their absolute orientations are of no importance for image reconstruction purposes and no attempt will be made to determine them.

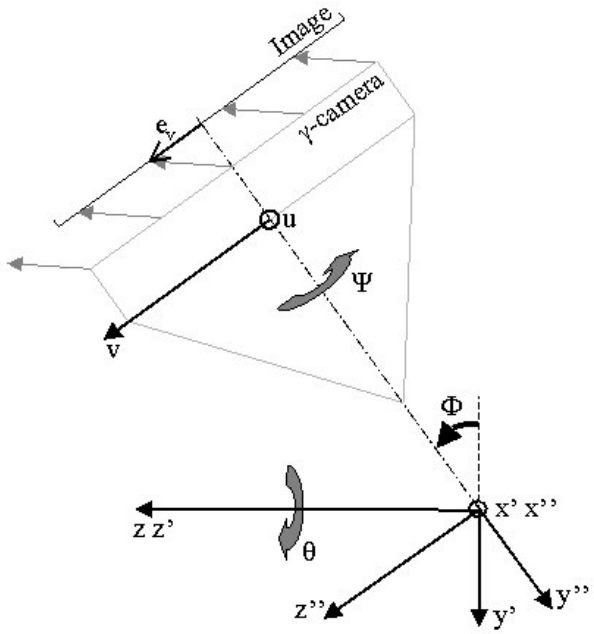

Fig. 2. The rotations θ, Φ and Ψ about the z-, x'- and y''-axis respectively, and the effect of the electrical offset e_v on the image formation. The geometry shown is for $\Psi = 0$. The symbol ◯ indicates axes perpendicular to the figure.

The orientation of the uv-system (detector) can be further specified by two additional angles, namely the tilt Φ and the twist Ψ (cfr. figure 1, 2). The tilt Φ represents the angle between the detector and the rotation axis. A camera may be tilted deliberately to bring the focal point close to a target organ, but in a way that allows the camera to clear other parts of the body [1]. The tilt can be taken into account by rotating the $x'y'z'$-system over the tilt angle Φ to obtain the $x''y''z''$ coordinate system. This rotation is performed about the x'-axis and as a result, both the x''- and z''-axis are parallel to the detector surface.

$$\begin{bmatrix} x'' \\ y'' \\ z'' \end{bmatrix} = \begin{bmatrix} 1 & 0 & 0 \\ 0 & cos\Phi & -sin\Phi \\ 0 & sin\Phi & cos\Phi \end{bmatrix} \begin{bmatrix} x' \\ y' \\ z' \end{bmatrix} \qquad (2)$$

The twist Ψ represents the angle between the u-axis and the direction on the detector surface perpendicular to the rotation axis. It is the orientation angle of the pixels on the detector surface. Since the x''-axis is still parallel to the detector surface and orthogonal to the rotation axis, the twist angle Ψ is also the angle between the u- and x''-axis. Rotating the $x''y''z''$-system over this angle Ψ, finally yields the $x'''y'''z'''$ coordinate system, with the x'''- and z'''-axis parallel to the u- and v-axis respectively.

$$\begin{bmatrix} x''' \\ y''' \\ z''' \end{bmatrix} = \begin{bmatrix} cos\Psi & 0 & -sin\Psi \\ 0 & 1 & 0 \\ sin\Psi & 0 & cos\Psi \end{bmatrix} \begin{bmatrix} x'' \\ y'' \\ z'' \end{bmatrix} \qquad (3)$$

Figure 2 summarizes the rotations of the xyz coordinate system to align it with the uv-system. The geometry shown is for $\Psi = 0$.

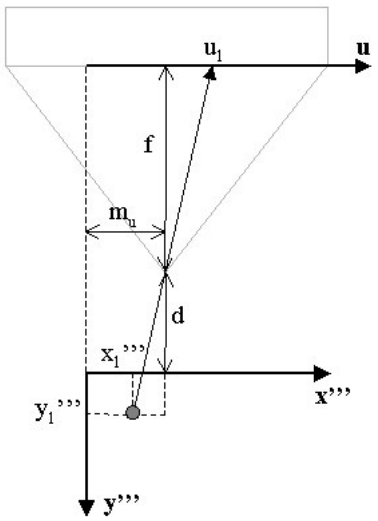

Fig. 3. Projection of Point Source (x_1,y_1,z_1), seen in z'''-direction.

After application of the above rotations, the camera-image geometry can further be described by the distances f, d and m, as illustrated in figure 1. The distances f and d are measured along the central ray and represent respectively the focal length and the distance between the focal point and the plane parallel to the detector and through the xyz-origin. The mechanical offset m is the distance between the central ray and the rotation axis. By definition this distance is measured in the direction orthogonal to the rotation axis and parallel to the detector surface, like the x'-axis (x''-axis). Thereby, it forms the angle Ψ with the u-axis and the length can be decomposed into its uv-components (m_u, m_v).

$$\begin{aligned} m_u &= m\cos\Psi \\ m_v &= m\sin\Psi. \end{aligned} \tag{4}$$

The origin of the xyz-system is chosen such along the z-axis that the central ray intersects the x'-axis (x''-axis). Thereby, the mechanical offset m can be measured as the distance between the xyz-origin and the central ray. Since the uv-origin was defined as the orthogonal projection of the xyz-origin, the offset m can equivalently be measured as the distance between the uv-origin and the central ray. Here the xyz-origin has been defined with respect to the focal point and detector positions, instead of defining their absolute positions in space. Once again, this absolute reference is of no importance for image reconstruction.

B. Point source Projection

Using the parameters and coordinate systems of the above section, the pinhole projection of a point source (x, y, z) can be calculated. The projection is defined by its coordinates (u_θ, v_θ) in the uv coordinate system. Based on congruent triangles, illustrated in figure 3, the following equations hold:

$$\frac{x''' - m_u}{d + y'''} = \frac{m_u - u_\theta}{f} \tag{5}$$

$$\frac{z''' - m_v}{d + y'''} = \frac{m_v - v_\theta}{f}. \tag{6}$$

Rearranging them and inserting equations (4) yields

$$u_\theta = f\frac{m\cos\Psi - x'''}{d + y'''} + m\cos\Psi \tag{7}$$

$$v_\theta = f\frac{m\sin\Psi - z'''}{d + y'''} + m\sin\Psi. \tag{8}$$

The projections (u_θ, v_θ) are defined in the uv coordinate system, but the projection location of the uv-origin in the projection images is unknown and can be affected by an electrical shift. This electrical shift causes a collective translation of all detector locations (u_θ, v_θ) to the projection image locations $(u_\theta^{img}, v_\theta^{img})$, as illustrated in figure 2. The projection location of the uv-origin can however be described by the coordinates (e_u, e_v) with respect to some known point in the projection image, like for example the center of the image. Using these coordinates, the other point source locations can be corrected as well:

$$u_\theta^{img} = f\frac{m\cos\Psi - x'''(\theta,\Phi,\Psi)}{d + y'''(\theta,\Phi,\Psi)} + m\cos\Psi + e_u \tag{9}$$

$$v_\theta^{img} = f\frac{m\sin\Psi - z'''(\theta,\Phi,\Psi)}{d + y'''(\theta,\Phi,\Psi)} + m\sin\Psi + e_v. \tag{10}$$

C. Projection Information

The above equations (9) and (10) express the point source projections $(u_\theta^{img}, v_\theta^{img})$ in function of the rotation angle θ, the point source coordinates x, y, z and the geometrical parameters f, d, m, e_u, e_v, Φ and Ψ. The calibration procedure under study poses the inverse problem of determining the values of f, d, m, e_u, e_v, Φ and Ψ from the measurement of a set of point sources. The position of these point sources is unknown as well. Otherwise the calibration phantom would have to be positioned carefully under the camera or additional measurements to determine those locations would be required. However, assuming a rigid calibration phantom, the distances between its different point sources are fixed and known.

This section investigates how much information the projections of a point source provide about the camera geometry. It determines the minimum number of point sources yielding a unique solution of the calibration problem and the restrictions on the point source locations in the field of view. It does so by equating the relations (9) and (10) expressed in function of two different sets of parameters and coordinates

$$f, d, m, e_u, e_v, \Phi, \Psi, \text{ and} \\ x_i, y_i, z_i \text{ with } i = 1, 2, ..., I \tag{11}$$

$$\widetilde{f}, \widetilde{d}, \widetilde{m}, \widetilde{e_u}, \widetilde{e_v}, \widetilde{\Phi}, \widetilde{\Psi} \text{ and} \\ \widetilde{x_i}, \widetilde{y_i}, \widetilde{z_i} \text{ with } i = 1, 2, ..., I \tag{12}$$

for an increasing number of point sources I. The resulting set of relations is then solved for the first set of parameters

and coordinates in function of the second set. The calibration problem has a unique solution if it is found that the two sets of parameters and coordinates have to be identical. This means that no false set of parameters and point source locations can be found yielding the same projection locations $(u_{i\theta}^{img}, v_{i\theta}^{img})$ as the correct set.

Before starting, it is convenient to transform the Cartesian coordinates $x_i y_i z_i$ into cylindrical coordinates

$$r_i = \sqrt{x_i^2 + y_i^2} \quad (13)$$

$$\alpha_i = \arctan\left(\frac{y_i}{x_i}\right) \quad (14)$$

$$z_i = z_i. \quad (15)$$

Using these coordinates, the right hand sides of equations (9) and (10) expressed in the different sets of parameters and coordinates are set equal to each other. The resulting relations must be satisfied for every projection angle θ. Assuming however a sufficiently large number of projections angles, this is equivalent to satisfying those relations for arbitrary projection angles θ. For point sources located off the axis of rotation, the appendix demonstrates that this yields the set of equations

$$\widetilde{\Psi} = \Psi, \quad (16)$$

$$\widetilde{f} = f\frac{\cos\widetilde{\Phi}}{\cos\Phi}, \quad (17)$$

$$\widetilde{\alpha_i} = \alpha_i \quad i = 0, 1, ..., I\ , \quad (18)$$

$$\frac{\widetilde{z_i}}{\widetilde{r_i}} = a\frac{z_i}{r_i} + b\frac{d}{r_i} \quad i = 0, 1, ..., I\ , \quad (19)$$

$$\frac{\widetilde{d}}{\widetilde{r_i}} = b\frac{z_i}{r_i} + a\frac{d}{r_i} \quad i = 0, 1, ..., I\ , \quad (20)$$

$$\frac{\widetilde{m}}{\widetilde{r_i}} = \frac{m}{r_i} \quad i = 0, 1, ..., I\ , \quad (21)$$

$$(\widetilde{m} - m)\cos\Psi + (\widetilde{e_u} - e_u) = f\frac{\sin\Psi}{\cos\Phi}(\sin\Phi - \sin\widetilde{\Phi}), \quad (22)$$

$$(\widetilde{m} - m)\sin\Psi + (\widetilde{e_v} - e_v) = -f\frac{\cos\Psi}{\cos\Phi}(\sin\Phi - \sin\widetilde{\Phi}) \quad (23)$$

with

$$a = \frac{1 - \sin\Phi\sin\widetilde{\Phi}}{\cos\Phi\cos\widetilde{\Phi}}, \quad (24)$$

$$b = \frac{\sin\widetilde{\Phi} - \sin\Phi}{\cos\Phi\cos\widetilde{\Phi}}. \quad (25)$$

First consider equation (20). Since both $\widetilde{d} > 0$ and $\widetilde{r_i} > 0$, the right hand side of equation (20) must be strictly positive as well. Since $\Phi \in \left]-\frac{\pi}{2}, \frac{\pi}{2}\right[$, it can be easily shown that this is always true for $|z_i| < d$, which will normally be satisfied because of the limited field of view of a pinhole camera. Furthermore, for $|z_i| \geq d$, it can still be shown that there is always a range of values of $\widetilde{\Phi}$ for which the above remark is satisfied. This range narrows with larger values of $|\Phi|$ and $|z_i|$, but is still approximately equal to $\left]-\frac{\pi}{2}, \frac{\pi}{2}\right[$ for any practical values of $|\Phi|$ and $|z_i|$. Therefore, we can neglect this constraint in the rest of the calculations.

With $I = 1$, the relations (16) to (23) show that different sets of parameters can describe the same tomographic projection of a single point source. The parameters Ψ and α always have to be identical, as shown by equations (16) and (18). But, equation (17) and (19) to (21), allow to calculate the values of $\widetilde{f}$, $\widetilde{z}$, $\widetilde{d}$ and $\widetilde{m}$ respectively in function of arbitrary values of $\widetilde{\Phi}$ and $\widetilde{r}$ and the true geometrical parameters. Equations (22) and (23) finally determine the values $\widetilde{e}_u$ and $\widetilde{e}_v$ respectively.

Consider now the projection of two point sources at location $r_1\alpha_1 z_1$ and $r_2\alpha_2 z_2$, with $z_1 \neq z_2$, by a pinhole camera. The equations (16) to (23) still hold, but now for $I = 2$. With $m \neq 0$ and $\widetilde{m} \neq 0$, it is easy to prove that these relations can only hold for $\widetilde{\Phi} = \Phi$ and that

$$\frac{z_1}{\widetilde{z_1}} = \frac{z_2}{\widetilde{z_2}} = \frac{r_1}{\widetilde{r_1}} = \frac{r_2}{\widetilde{r_2}} = \frac{d}{\widetilde{d}} = \frac{m}{\widetilde{m}}. \quad (26)$$

The above relation only allows a scaling of the r- and z-coordinates of the point source locations. The distance between the two point sources will be scaled as well. However, the knowledge of the distance between the two point sources can be used to constrain the solution to the ones with the correct distances, leaving only the trivial solution possible. Thereby, two point sources provide sufficient information for the complete calibration of a pinhole camera, if the mechanical offset m of the camera is non-zero. However, for a normal pinhole camera, the mechanical offset may be assumed to be small and so a normal pinhole camera agrees reasonably well with the special case of $m = 0$. In that case the equations (16) to (23) can be satisfied for an arbitrary value of $\widetilde{\Phi}$ and for an arbitrary number of point sources I.

As mentioned before, the distances between different point sources yield additional relations, that can be used to constrain the solutions. For two different point sources i and k, the conservation of the distance between them yields the relation

$$(z_i - z_k)^2 + r_i^2 + r_k^2 - 2r_i r_k\cos(\alpha_i - \alpha_k) = (\widetilde{z_i} - \widetilde{z_k})^2 + \widetilde{r_i}^2 + \widetilde{r_k}^2 - 2\widetilde{r_i}\widetilde{r_k}\cos(\alpha_i - \alpha_k) \quad (27)$$

The parameters $\widetilde{z_i}$, $\widetilde{z_k}$, $\widetilde{r_i}$ and $\widetilde{r_k}$ can be written in function of $\widetilde{d}$ using the equations (19) and (20). Substituting them in equation (27) and solving for $\widetilde{d}$ yields

$$\widetilde{d} = g_i g_k \sqrt{\frac{(z_i - z_k)^2 + r_i^2 + r_k^2 - 2r_i r_k\cos(\alpha_i - \alpha_k)}{(z_i - z_k)^2 d^2 + r_i^2 g_k^2 + r_k^2 g_i^2 - 2r_i r_k g_i g_k\cos(\alpha_i - \alpha_k)}} \quad (28)$$

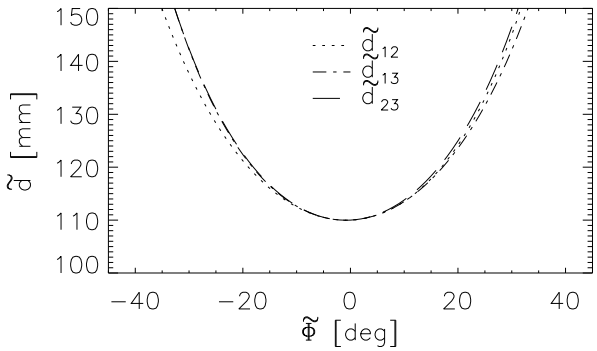

Fig. 4. Parameter $\widetilde{d}$ in function of $\widetilde{\Phi}$ for a unfavorable point source configuration.

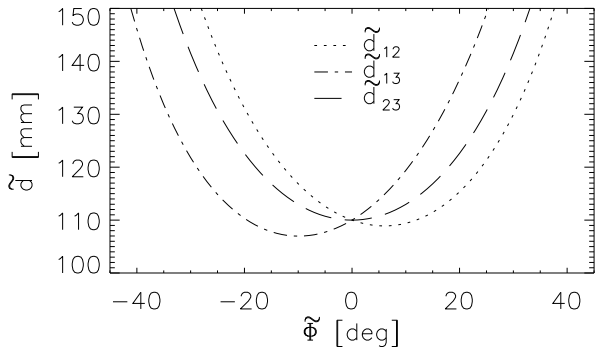

Fig. 5. Parameter $\widetilde{d}$ in function of $\widetilde{\Phi}$ for a favorable point source configuration.

with

$$g_i = b\, z_i + a\, d \tag{29}$$

and a and b as defined by equations (24) and (25). It is easy to show that $\widetilde{d}$ has always a real solution for an arbitrary value of $\widetilde{\Phi}$. Thereby, with $m = 0$, it is possible to calculate a false set of parameters to describe the tomographic projection data of two point sources, even if the distance between the points is fixed at the correct value.

Finally consider the three point source case. The distances between these point sources yield three different equations (like equation (28)) to calculate the value of $\widetilde{d}$. Of course, only those solutions that yield the same solution of $\widetilde{d}$ by all three equations are acceptable. Equation (28) shows that this depends on d and on the point source locations r_i, α_i, z_i for $i = 1, 2, 3$. It is easy to prove that a common value of $\widetilde{d}$ is always found if

$$z_1 = z_2 = z_3. \tag{30}$$

So three point sources located at the same z-location form an inappropriate phantom to calibrate a pinhole camera. Assuming three different z-locations, it is unclear whether point source configurations exist yielding a common value of $\widetilde{d}$ for arbitrary values of $\widetilde{\Phi}$. However, there are certainly point source configurations, that yield nearly the same value of $\widetilde{d}$ for a broad range of $\widetilde{\Phi}$-values. From a calibration perspective, these geometries are equally unfavorable. This can be checked prior to calibration by plotting the right hand side $\widetilde{d}_{ik}$ of equation (28) in function of $\widetilde{\Phi}$ for the different point source combinations ik. At $\widetilde{\Phi} = \Phi$ the different curves cross or touch each other at exactly the same point. For a configuration of point sources to be suitable for calibration, at least two of the curves should cross each other at a sufficiently large angle. Figure 4 and 5 show two examples of such curves for the point source configurations of table II. The point source configuration of figure 4 yields large variances for the parameters Φ and e_v, while the configuration of figure 5 yields good results.

TABLE II
Point Sources Configurations used in Fig. 4 and 5.

Fig nr.	Point nr.	x [mm]	y [mm]	z [mm]
4	1	-30.0	0.0	-10.8
	2	-35.0	0.0	0.0
	3	-30.0	0.0	13.9
5	1	-30.0	0.0	-33.5
	2	-35.0	0.0	-8.5
	3	-30.0	0.0	33.5
$d = 110\,\text{mm},\ \Phi = 0.0\,\text{deg}$				

D. Parameter Estimation

To estimate the geometry of a pinhole camera, we select an appropriate point source configuration, as described above. In principle, this requires knowledge of the point source locations, the distance d and the tilt Φ. We assume however that estimates of these parameter values with limited accuracy provide sufficient information for this purpose. The resulting configuration serves as the calibration phantom and a tomographic set of projections is obtained from it over J projection angles θ_j $(j = 1, 2, ..., J)$. Since the above equations (9) and (10) provide very good approximations for the relation between the mass center of a physical point source and that of its pinhole projection [17], a set of projection data $(u_{ij}^{img}, v_{ij}^{img})$ is obtained as the projection mass centers of each point i at each angle j. These data are fitted to ideal, calculated data $(u_{ij}^{est}, v_{ij}^{est})$ based on estimates of the point source locations and the geometrical pinhole parameters. The goodness of fit is evaluated by the least square cost function F. This cost function sums the squared distances between the estimated and measured point source projection locations. Better estimates lead to smaller distances, eventually leading to $F = 0$ for a perfect fit.

$$F = \sum_i \sum_j \left[\left(u_{ij}^{img} - u_{ij}^{est} \right)^2 + \left(v_{ij}^{img} - v_{ij}^{est} \right)^2 \right]. \tag{31}$$

The minimization of F is performed with Powell's method. This is a direction set method for the multidimensional minimization of functions. The minimization of an N-variable function is performed by repeated cycles of N successive one-dimensional line minimizations along conjugate directions [23].

The choice of the calibration phantom assures that only the correct pinhole and point source geometry can be found as a valid solution that minimizes the above function F. Therefore, the correct distances between the different point sources are imposed on the solution. This is done by expressing the point source coordinates x_i, y_i, z_i with $i = 1, 2, 3$ in function of the distances $\overline{12}, \overline{13}, \overline{23}$ between the point sources. To do so, consider the calibration phantom as a triangle with the three point sources located in the vertices. The known distances $\overline{12}, \overline{13}, \overline{23}$ define the shape of the triangle. The triangle can be placed at an arbitrary position in the xyz space by three translations and three rotations. Only the translations and rotations have to be fitted. Further, the parameters f, d, Φ and Ψ can be measured up to some reasonable accuracy. They are used to constrain the result by specifying intervals in which the parameter estimate is acceptable. For a parameter estimate outside such interval, the cost function is evaluated in the closest acceptable value of the parameter and a penalty proportional to the squared difference between the estimate and the acceptable value is added to the result. This drives the algorithm back to the acceptable parameter range.

III. Experiments

A. Calibration Phantom

The tomographic projection data of the calibration phantom must contain sufficient information to enable the correct determination of the complete acquisition geometry. Noo *et al.* [21] already observed that for this purpose more than two point sources are necessary. This observation was confirmed by the calculations in the previous chapter. The first experiment illustrates that at least three point sources are necessary. For that purpose, the ideal projection data of two point sources are simulated and used to perform a camera calibration, while fixing one parameter at a wrong value. A configuration of point sources provides sufficient information if no false set of parameter values can be found that yields exactly the same projection data set $(u_{1\theta}^{img}, v_{1\theta}^{img})$, as discussed in the theory. The experiment shows that such false data sets can easily be found for the two point source case, as predicted in the previous chapter. The results obtained from the above fitting procedure are compared with results from an analytical procedure. The latter method calculates the pinhole parameters using the equations (16) to (23) and (28) with $m = 0$.

The experiment is performed for a pinhole camera with a focal length f of 240 mm and a distance d equal to 110 mm. The other pinhole parameters, including the mechanical offset m, are all equal to zero. The two point sources are located at $x = -33.0$ mm, $y = 0.0$ mm and at $z = -33.5$ mm or $z = 33.5$ mm. The simulation is performed for 64 equidistant projection angles.

B. Estimation Accuracy

In combination with noise, the correlations between the geometric parameters can affect the estimation accuracy. The centroids of the projected point sources can however be accurately measured, except for any systematic errors [15], yielding low uncertainties about the projection locations. To evaluate the parameter estimation accuracy, the second experiment calculates the means, standard deviations and cross-correlations of the parameter estimates from 100 simulations of calibration data sets. For two sample populations $(x_0, x_1, ..., x_N)$ and $(y_0, y_1, ..., y_N)$, with means $\bar{x}$ and $\bar{y}$ respectively, the cross-correlation P_{xy} is defined as

$$P_{xy} = \frac{\sum_{k=0}^{N} (x_k - \bar{x})(y_k - \bar{y})}{\sqrt{\left[\sum_{k=0}^{N} (x_k - \bar{x})^2\right]\left[\sum_{k=0}^{N} (y_k - \bar{y})^2\right]}}. \quad (32)$$

The data sets are obtained by adding Gaussian noise with 0.2 mm or 0.3 mm standard deviation, to the exact point source projection coordinates, calculated with equations (9) and (10) for 64 equidistant projection angles. These standard deviations were chosen approximately 2 and 3 times larger then the statistical errors obtained by Gullberg *et al.* [15]. For still larger standard deviations, the shape of the 'elliptical' paths of the point source projections in the projection image is visually more disturbed than the shape of a measured path. The camera- and phantom geometries used, are similar to those used for the real phantom measurements and are listed in table III. Note that the curves of figure 5 have been generated for this geometry. The table also contains the initial values with which the estimation process is started and the constraints for the parameters f, d, Φ and Ψ.

The variances and covariances of the parameter estimates can also be approximated analytically. For that purpose, the equations (9) and (10) are approximated by a linear Taylor series expansion about the true parameter values and point source coordinates, taking into account that the distances between the point sources are fixed. This yields a linear system

$$U = U_0 + M\,\Delta P \quad (33)$$

where U_0 is a vector with the u_{ij}^{img} and v_{ij}^{img} measurements obtained at the expansion point. The matrix M contains the first derivatives of the equations (9) and (10) evaluated at the expansion point and the vector ΔP contains the deviation from the expansion point. Such deviation yields the measurement U instead of U_0. The substitution of equation (33) into equation (31) yields a linear estimator minimizing the function F. The covariances of the parameters $\mathrm{cov}(P)$ can be approximated by propagating

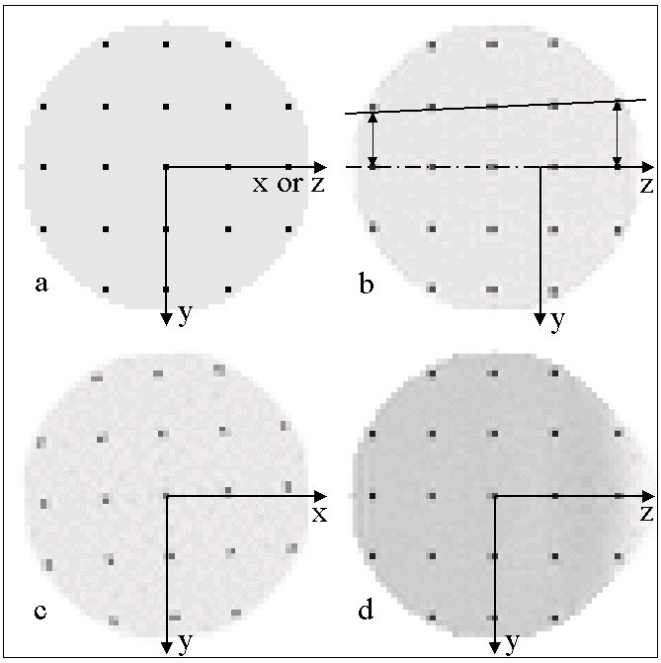

Fig. 6. Reconstruction Accuracy. (a) Central slice of the software phantom. (b) Reconstruction of the yz plane of the phantom, with the calibration estimate of Φ fixed at -6.0 deg instead of 0.0 deg. The radial scaling along the rotation axis is indicated by the double arrows in the upper part of the image. The translation along the rotation axis is visible from the seemingly displaced yz-origin. (c) Reconstruction of the xy plane of the phantom, with the calibration estimate of m fixed at -7.5 mm instead of 0.0 mm ($\Phi = 0.0$ deg). (d) Reconstruction of the yz plane of the phantom, with the calibration estimate for f fixed at 223.3 mm instead of 240.0 mm ($\Phi = -25.0$ deg). The background has been set to twice the normal value for better visualization of the under sampling artifact.

the covariances of the data $\mathrm{cov}(U)$ through this linear estimator, yielding

$$\mathrm{cov}(P) = (M^T M)^{-1} M^T \mathrm{cov}(U)\, M (M^T M)^{-1}. \qquad (34)$$

The parameter cross-correlations are easily obtained by dividing each column and each row of $\mathrm{cov}(P)$ by the square root of its diagonal element. The approximated standard deviations and cross-correlations are compared with those obtained from the fitting procedure.

C. Reconstruction Accuracy

This third experiment relates estimation errors to the estimation residue and the image reconstruction accuracy. For this purpose a software phantom is created. The phantom consists of a sphere, containing background activity, with a cubic grid of point sources (pixels with high activity) inside. The contrast (highest activity level divided by lowest activity level) between the point source and background activity equals 10. The sphere has a diameter of 72.8 mm and the distance between neighboring point sources is 15.4 mm. The sphere is discretized into pixels of 1.4 mm. In total the sphere contains 57 point sources. Figure 6a shows the central slice of this phantom.

Using the camera- and calibration phantom geometries already listed in table III, the tomographic data of the sphere and the calibration phantom are simulated for 64 equidistant projections of 128x128 pixels of 1.695 mm, using a ray driven projector. With one parameter held at a wrong value and using the initial values and constraints of table III for the other parameters, an estimate of the camera geometry is calculated. Using this estimate, an OS-EM reconstruction [24–26] of the sphere phantom is made and compared to the original image. The reconstruction used an iteration scheme with a decreasing number of subsets: 10x8, 8x4 and 5x1, where the first figure denotes the number of OS iterations and the second one the number of subsets. The reconstructed image is registered to the original image by translation and rotation, by a least squares minimization of the distances between the original and reconstructed point sources. In this experiment, the average distance between the original and reconstructed point sources provides a measure of the reconstruction accuracy, while the errors of the fixed parameter values relate to the estimation accuracy. Both measures are compared to the calibration residue, which is the only measure available in practice.

D. Phantom Measurement

To evaluate the performance of the calibration method with real data, a phantom was developed consisting of a grid of 16 point sources. The grid can be divided into three slices of 5 point sources. The point sources are approximately located in the vertices and the center of a 5 cm by 5 cm square. The distance between the different slices is approximately 2.5 cm. One extra point source is added to allow the unique identification of every point source in reconstructed images.

Using our GE Millennium MPR camera with approximately the camera- and calibration phantom geometries listed in table III and a tungsten knife-edge [27] pinhole aperture of 3 mm, a tomographic acquisition of the phantom was performed with 64 equidistant 60 s projections of 128x128 pixels of 1.695 mm. The phantom point sources contain approximately 1.85 MBq ^{99m}Tc in 2.5 μL water. Without repositioning the camera, an identical acquisition, but with 25 s projections, is performed of the calibration phantom, which contains three 3.7 MBq ^{99m}Tc point sources in 5.0 μL water. The data of the second acquisition are used to calibrate the camera. This allows to reconstruct the grid phantom from the data of the first acquisition. The reconstruction is performed with an OS-EM algorithm with compensation for the pinhole sensitivity [27]. The reconstruction used an iteration scheme with a decreasing number of subsets: 10x8, 10x4 and 5x1, where the first figure denotes the number of OS iterations and the second one the number of subsets. The reconstruction pixel size is 1.4 mm. The calibration is performed using the initial values and constraints of table III. The distances between the different point sources of the original phantom and of its reconstruction are measured and compared distance by distance. The differences between the measured and reconstructed distances provide a mea-

sure of the reconstruction accuracy. The resolution of the reconstructed point sources is also investigated.

IV. Results

A. Calibration Phantom

Consider the ideal pinhole camera with f and d equal to 240.0 mm and 110.0 mm respectively. For the case of two point sources, the calibration with e_v fixed at a wrong value results nevertheless in a perfect fit. For a linear variation of e_v from -10.0 mm to 10.0 mm, in steps of 2.5 mm, the detector tilt varies linearly from -2.4 deg to 2.4 deg. The parameters f and d show some submillimeter variation as well. Similar results are obtained by fixing Φ at a wrong value and allowing the parameter e_v to be fitted. These results are confirmed by the analytical calculations, based on equations (16) to (23) and (28). The above variations clearly indicate that the tomographic projection data of two point sources contain insufficient information for the complete calibration of a pinhole camera with circular detector orbit. Using the projection data of three point sources, the experiment was repeated both for 0.0 and -25.0 deg tilt. Consecutively, every parameter was fixed to four different values, with increasing error, but none of the attempts resulted a perfect fit using the incorrect parameter estimate, as predicted by the theory. The three point source case is discussed in more detail in section C 'Reconstruction Accuracy'.

B. Estimation Accuracy

Table III presents the mean μ_{CR} and standard deviation σ_{CR} of the calibration residue CR. This calibration residue CR is expressed as the average distance between the simulated and estimated point source projections after calibration. The residue is very closely centered around its mean value. It does not change with the detector tilt, but differs for different noise levels. The table also presents the standard deviations of the parameter estimates. Those are calculated both using the series of noisy simulations (upper values in table III) and by the analytical approximation of equation (34) (lower values in table III). All estimates are centered around the correct solution, but the spread differs for the different parameters. The largest errors are found for the distances e_u and e_v, and for the tilt angle Φ. The simulated and approximated standard deviations are in very good agreement. A close inspection of the analytically approximated standard deviations indicates slightly larger values of the estimates of tilted geometries than of non-tilted geometries. The largest differences are found for the parameters d and e_v, but remain nevertheless under 0.04 mm for 0.3 mm noise.

Table IV presents the cross-correlations of the parameter estimates, calculated for both 0.0 deg and -25.0 deg tilt and 0.3 mm noise. The results for the 0.2 mm noise cases are nearly identical. The cross-correlations from the analytical and fitting procedures are in good agreement with each other. The parameters m and e_u, and e_v and Φ are highly correlated. The parameters f and d are highly correlated for 0.0 deg tilt, but to a lesser extent for the -25.0 deg tilt case. In the latter case, there is an additional correlation between the distance d and the parameters e_v and Φ. Finally, the twist Ψ shows no clear correlations with any other parameter for the 0.0 deg tilt case. For Φ = -25.0 deg however, there is strong correlation with the parameters m and e_u. The above mentioned correlations are indicated in bold in table IV.

TABLE V
Calibration Residues and Reconstruction Errors in function of the Estimate Error of Ψ (Φ = -25.0 deg).

$\Delta\Psi$ [deg]	CR [mm]	RE [mm]
-0.20	0.09	0.04
-0.40	0.19	0.07
-0.60	0.28	0.08
-0.80	0.38	0.08
-1.00	0.47	0.08
-1.20	0.56	0.07
-1.40	0.66	0.10
-1.60	0.75	0.12
-1.80	0.84	0.13
-2.00	0.93	0.11

C. Reconstruction Accuracy

Figure 7 shows the reconstruction error RE as a function of the calibration residue CR, for calibrations performed with one parameter estimate fixed at a wrong value. The calibration residue CR is again defined as the average distance between the estimated and measured projections of the calibration point sources. The reconstruction error RE is defined as the average distance between the original and reconstructed point sources in the software phantom. The different symbols in the figure indicate the different parameters, of which the estimate is fixed at 4 different values, with increasing errors with respect to the correct value. These errors are given in the table included in figure 7 and were chosen to yield calibration residues of approximately 1 mm and less, since real calibration measurements indicated this limit to be easily obtainable. For all parameters, the calibration residues increase with increasing errors. The residues show no large differences between the 0.0 and -25.0 deg tilt case, except for the parameter Ψ. The estimate errors only cause sub-pixel reconstruction errors which are less than the calibration residue. Table V shows that this also holds for estimate errors of the twist Ψ larger than -1.6 deg in the -25.0 deg tilt case. Fixing the parameter estimates of e_v or Φ to a wrong value results in the largest reconstruction errors. The reconstruction errors must be interpreted carefully, since the error on these sub-pixel values can be of the same magnitude as the reconstruction errors themselves.

Visual inspection of the reconstructed images shows that errors on the parameters e_v and Φ cause the reconstructed image to be translated along the axis of rotation with

TABLE III
Estimation Accuracy.

True stands for the real camera and calibration phantom geometry, init for the initial estimates, and constraint for the parameter estimate bounding limits. Upper standard deviations are based on simulations; lower standard deviations are based on the analytic approximation.

Calibration Point Source Locations									
	x_1 [mm]	y_1 [mm]	z_1 [mm]	x_2 [mm]	y_2 [mm]	z_2 [mm]	x_3 [mm]	y_3 [mm]	z_3 [mm]
true	-30.0	0.0	-33.5	-35.0	0.0	-8.5	-30.0	0.0	33.5
init	0.0	0.0	0.0	0.0	0.0	25.5	0.0	13.2	65.7

Camera Geometry									
	f [mm]	d [mm]	m [mm]	e_u [mm]	e_v [mm]	Φ [deg]			Ψ [deg]
true	240.0	110.0	0.0	0.0	0.0	0.0	or	-25.0	0.0
init & constraint	250.0 ±50.0	120.0 ±50.0	1.8	-0.4	0.8	-1.6 ±10.0	or	-26.6 ±10.0	0.3 ±5.0

Calibration Residue CR			**Parameter Estimate Standard Deviations**						
Tilt & Noise level	μ_{CR} [mm]	σ_{CR} [mm]	f [mm]	d [mm]	m [mm]	e_u [mm]	e_v [mm]	Φ [deg]	Ψ [deg]
Φ = 0.0 deg	0.25	0.01	0.2	0.1	0.1	0.3	0.4	0.10	0.01
σ = 0.2 mm			0.3	0.1	0.1	0.4	0.4	0.10	0.01
Φ = 0.0 deg	0.37	0.01	0.3	0.2	0.2	0.5	0.6	0.16	0.02
σ = 0.3 mm			0.4	0.2	0.2	0.5	0.6	0.14	0.02
Φ = -25.0 deg	0.25	0.01	0.3	0.1	0.1	0.4	0.4	0.10	0.03
σ = 0.2 mm			0.3	0.1	0.1	0.4	0.4	0.10	0.03
Φ = -25.0 deg	0.37	0.01	0.4	0.2	0.2	0.5	0.7	0.16	0.04
σ = 0.3 mm			0.4	0.2	0.2	0.5	0.7	0.14	0.04

respect to the original image. Additionally, the reconstructed image is slightly scaled in radial direction according to the position along the axis of rotation, as shown in figure 6b. Inspection of the parameter estimates again shows these parameters to be strongly correlated. Another prominent correlation exists between the parameters m and e_u and errors on them cause the reconstructed images to be rotated around the axis of rotation. There is however no sign of a real image distortion. A reconstruction of the central slice of the phantom is shown in figure 6c. Errors on the other parameters visually have a less prominent influence on the reconstructed images. Besides the effects of estimate errors, all reconstructions of the -25.0 deg tilt case show an artifact due to the insufficient sampling of the back region of the phantom. The artifact is clearly visible in the right side of figure 6d.

D. Phantom Measurement

For each acquisition of the grid of point sources (Φ = 0.0 deg and Φ = -25.0 deg), two calibration measurements, with intermediate repositioning of the calibration phantom, were performed. The repositioning of the calibration phantom provides two independent calibration measurements of the same camera geometry and with the calibration point sources at approximately the same location. The results of the camera calibrations are listed in table VI. The calibration residue is approximately 0.5 mm in all four cases. The parameter estimates for the same camera geometries show some little differences, as expected due to the parameter correlations. The distances between the point sources in the different reconstructions (based on different calibration measurements) of the same projection data, are however identical up to 0.1 mm for both tilt cases. When comparing the distances with those measured on the actual phantom, the largest difference found was 1.0 mm for -25.0 deg tilt and 1.3 mm for 0.0 deg tilt. Most differences are however much smaller. The distances between the point sources of the real phantom have been measured with an accuracy of approximately 0.3 mm.

The difference in coordinates of the estimated and measured point source projections after calibration, is not entirely random and shows similarities for the three calibration point sources. This is illustrated in figure 8 by the differences for the u coordinates of the projections of the three calibration point sources from the first calibration measurement with Φ = 0.0 deg.

The FWHM of the reconstructed point sources ranges from 4.0 to 5.0 mm.

V. Discussion

Like Noo *et al.* [21], we find that two calibration point sources provide insufficient information for the complete

TABLE IV
PARAMETER ESTIMATE CROSS-CORRELATIONS

Parameter Estimate Cross-correlation ($\sigma = 0.3\,\text{mm}$)								
Fitting		f	d	m	e_u	e_v	Φ	Ψ
$\Phi = 0.0\,\text{deg}$	f	**1.00**	**0.97**	-0.01	0.02	0.08	0.09	0.00
	d		**1.00**	0.01	-0.01	0.10	0.11	0.02
	m			**1.00**	**-1.00**	-0.11	-0.12	-0.14
	e_u				**1.00**	0.11	0.12	0.14
	e_v					**1.00**	**0.99**	-0.02
	Φ						**1.00**	-0.02
	Ψ							**1.00**
Analytical		f	d	m	e_u	e_v	Φ	Ψ
$\Phi = 0.0\,\text{deg}$	f	**1.00**	**0.97**	0.00	0.00	0.00	0.02	0.00
	d		**1.00**	0.00	0.00	-0.03	-0.05	0.00
	m			**1.00**	**-1.00**	0.00	0.00	-0.06
	e_u				**1.00**	0.00	0.00	0.06
	e_v					**1.00**	**0.98**	0.00
	Φ						**1.00**	0.00
	Ψ							**1.00**
Fitting		f	d	m	e_u	e_v	Φ	Ψ
$\Phi = -25.0\,\text{deg}$	f	**1.00**	**0.70**	0.00	0.00	0.23	0.29	0.11
	d		**1.00**	-0.11	0.10	**-0.51**	**-0.44**	-0.08
	m			**1.00**	**-1.00**	0.14	0.15	**0.88**
	e_u				**1.00**	-0.14	-0.15	**-0.88**
	e_v					**1.00**	**0.99**	0.24
	Φ						**1.00**	0.25
	Ψ							**1.00**
Analytical		f	d	m	e_u	e_v	Φ	Ψ
$\Phi = -25.0\,\text{deg}$	f	**1.00**	**0.69**	0.00	0.00	0.18	0.24	0.00
	d		**1.00**	0.00	0.00	**-0.54**	**-0.46**	0.00
	m			**1.00**	**-1.00**	0.00	0.00	**0.90**
	e_u				**1.00**	-0.00	-0.00	**-0.90**
	e_v					**1.00**	**0.95**	0.00
	Φ						**1.00**	0.00
	Ψ							**1.00**

TABLE VI
CAMERA CALIBRATION RESULTS.

Calibration Residue	**Parameter Estimates**							
	CR [mm]	f [mm]	d [mm]	m [mm]	e_u [mm]	e_v [mm]	Φ [deg]	Ψ [deg]
$\Phi \cong 0.0\,\text{deg}$	0.52	252.9	117.4	0.3	4.1	5.9	0.97	-0.13
	0.53	253.0	117.5	0.2	4.3	6.2	1.04	-0.12
$\Phi \cong -25.0\,\text{deg}$	0.46	253.9	128.4	2.2	-2.2	7.7	-23.23	0.19
	0.48	253.9	128.3	2.5	-3.0	8.2	-23.15	0.22

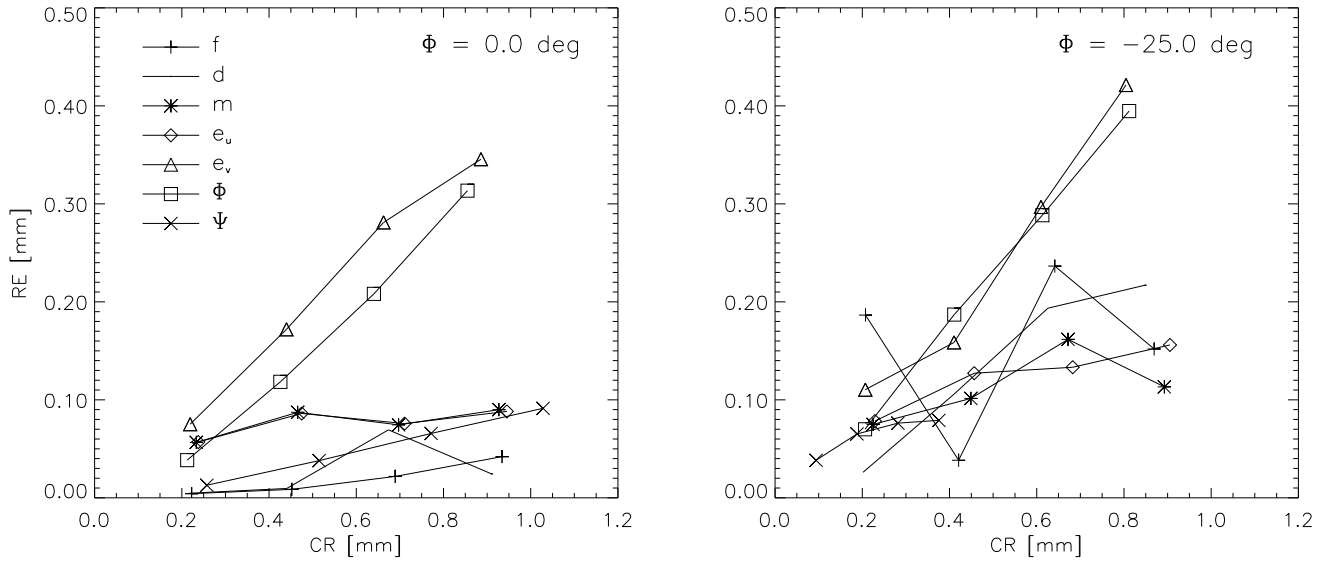

Parameter Estimate Errors						
Δf [mm]	Δd [mm]	Δm [mm]	Δe_u [mm]	Δe_v [mm]	$\Delta\Phi$ [deg]	$\Delta\Psi$ [deg]
-4.18	-5.75	-1.88	-6.25	-6.88	-1.50	-0.20
-8.35	-11.50	-3.75	-12.50	-13.75	-3.00	-0.40
-12.53	-17.25	-5.63	-18.75	-20.63	-4.50	-0.60
-16.70	-23.00	-7.50	-25.00	-27.50	-6.00	-0.80

Fig. 7. RE versus CR for the listed Estimate Errors

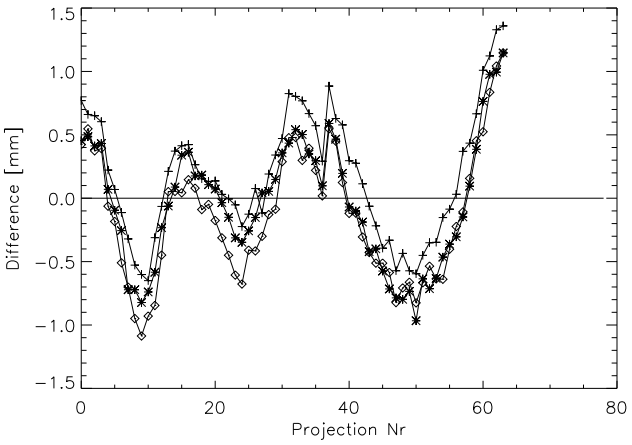

Fig. 8. The difference in u coordinates of the measured (u^{meas}) and estimated (u^{est}) calibration point source projections: ($u^{meas} - u^{est}$).

calibration of a pinhole camera. The addition of a third point source overcomes this problem, if the point sources are sufficiently well located, as shown in the theory. For the experiments, the three point sources are located on a slightly broken line, but approximately parallel to the rotation axis. This proved to be more stable than the use of a straight line, exactly parallel to the rotation axis. The last, rather theoretic, method occasionally yielded an outlier with respect to the results in table III. The point sources are located as far as possible from the axis of rotation and the two outermost sources are also located as far as possible from each other along the z-axis (axis of rotation). The third point source was finally located in between, but avoiding the plain of the focal point. In this arrangement, the outermost point sources satisfy the description of Noo *et al.* [21] about the ideal point source locations in his method. The location of the middle point source seems a logical extension of this for three point sources. However, placing the middle point source in the plane of the pinhole focus does not seem to cause any problems. Further, since a large number of projection angles over 360 deg are used in the calibration, the orientation of the point sources around the rotation axis was not assumed critical and the simplest geometry of a broken line was chosen. However, later experiments show standard deviations of the e_v and Φ estimates of almost half the original values for the middle point source rotated 180 deg around the rotation axis. The standard deviations of the other parameters seem unaffected by this rotation. Keeping in mind the results of figure 7, this should seriously reduce the reconstruction error. Surprisingly, this geometry shows a slightly worse crossing of the curves of $\widetilde{d}$ than the original geometry of figure 5. Finding the optimal calibration phantom geometry is a topic for future research. To find out whether additional calibration point sources could improve the performance, the second experiment has once been performed for four point sources. The results

are however very similar to the three point case.

As expected, some parameters are highly correlated. The correlated parameters e_v and Φ are clearly the most critical. The second experiment shows that noisy data cause the largest spread for the estimates of these parameters. Further, for the same calibration residue CR, the reconstruction errors RE are the largest for e_v and Φ, as shown in the third experiment. This causes these parameters to be the most difficult to estimate and it also causes the largest distortions of reconstructed images, when they are poorly estimated. From the image reconstruction point of view, not all correlations cause trouble however. Although noisy data also yield the largest standard deviation of the estimates of e_u, the reconstruction errors RE caused by e_u and m are only small.

The cross-correlations and their dependence on the tilt angle Φ can intuitively be explained from a number of geometrical considerations. First of all, for $m = 0$, the twist Ψ causes a rotation of the detector around the central ray. During acquisition, this rotation axis constantly changes, which explains why the twist can easily be estimated, yielding a small standard deviation of its estimate. A correlated error between m and e_u results in a rotation of the reconstructed image around the axis of rotation. For $\Phi = 0$, the central ray is always orthogonal to the rotation axis and no correlation between m, e_u and Φ exists. For a tilted detector however, the central ray is inclined towards the rotation axis, yielding a component of the rotation Φ along the rotation axis. This component along a common axis establishes the correlation between m, e_u and Φ. Secondly, the ratio of the focal length f and the distance d determines the magnification of the object in the field of view. This explains the correlation between f and d. The magnification is larger for parts of the object closer to the focal point. Because of the rotation of the focal point during acquisition, the magnification of parts of the object away from the rotation axis varies with the rotation angle θ. For larger tilt angles Φ this variation is less prominent, explaining the smaller correlation of f and d for such tilt angles. Finally, a correlated error between e_v and Φ, causes a translation of the reconstructed image along the z-axis. This changes the distance between the object and the focal point. For a tilted detector this also changes the magnification of the object, which is normally determined by the ratio of f and d. Thereby, additional correlations between the parameters f, d, e_v and Φ emerge.

For the simulation studies, the calibration method performs well and the calibration residue CR provides a conservative measure of the reconstruction accuracy that may be expected. For all badly estimated parameters, including e_v, the reconstruction error is always smaller than the calibration residue and in most cases even much smaller. Further, for the largest reconstruction errors, caused by e_v and Φ, the errors vary slowly throughout the reconstructed image, indicating a gentle deformation of the original distribution. Finally, because of sensitivity considerations, the geometries simulated in the experiments normally require a pinhole aperture of approximately 3 mm. The reconstruction errors presented in figure 7, are small with respect to this aperture size, which determines the resolution of the system.

For the real camera calibrations, the residue is approximately 0.5 mm. Figure 8 further illustrates that the individual distances between measured and calculated point source projections are not totally random and independent for different point sources. This suggests a systematic deviation of the camera geometry from the model presented. We observed a sudden, submillimeter displacement of our collimator during every acquisition. The effect of this displacement is small, but noticeable in the projection data set. However, it does not provide however a complete explanation for figure 8.

The effect of the imperfect calibration match was studied on reconstructions of real tomographic data of the grid of point sources. The small differences in parameter estimates for the same camera geometry, only result in negligible differences in the reconstructed images. The geometries in the reconstructed images were also compared to the real phantom geometry. Despite the measurement uncertainty, even the largest differences (1.0 mm for -25.0 deg tilt and 1.3 mm for 0.0 deg tilt) are small with respect to the pinhole aperture of 3 mm, which determines the resolution. The FWHM of the reconstructed point sources ranges between 4 mm and 5 mm and gives an indication of the system resolution. Because of the larger resolution, the errors will not cause any serious and noticeable degradation of the reconstructed image accuracy.

As mentioned in the theory, the values of the parameter estimates of f, d, Φ and Ψ were bounded during the experiments. This was done to guide the procedure to a useful solution. When starting with very poor initial estimates, the unbounded procedure sometimes lead to unrealistic solutions with very high calibration residues. The ranges of acceptable values were however sufficiently large to avoid any interference with the effects of the parameter correlations. Narrow parameter ranges, imposing strong a priori knowledge, are not always beneficial, since they may influence the convergence trajectory of the calibration procedure. For one of the real -25.0 deg tilt measurements, constraining the parameter Φ within ± 5 deg forced the procedure to stop before convergence with the estimate of Φ pinned at the limit of the acceptable values. The constraining of the same calibration within ± 10 deg converged without any problem.

The results presented above are specific for the acquisition geometries used. The difference in standard deviation of the estimate of Ψ between the 0.0 and -25.0 deg tilt case, provides a clear example of this. Due to the difference in tilt angle, there is a clear difference in the correlations between the parameters m, e_u and Ψ. The difference in correlation affects the standard deviation of the estimate. Fortunately, it has almost no effect on the reconstruction accuracy. The acquisition geometries studied are those of a perfect pinhole camera with a non-tilted or severely tilted detector. The variation of the tilt was chosen to cover the expected useful range of tilt values. Further, non-ideal

cameras have nonzero parameters m, e_u, e_v and Ψ. Deviations from this ideal case may however be expected to be small and the deviations of the calibration results are expected to be small as well. Thereby, only differences in the relative magnitude of f and d may cause a markedly different behavior from the above results. Especially for smaller distances d, since then even small values of m, e_u and e_v become relatively large. Our first experiments with small values of d (30 mm) show however promising results. As already mentioned, the use of a different calibration phantom can yield significantly different results.

VI. Conclusions

A new method for the calibration of a pinhole camera for image reconstruction purposes was presented. The tomographic projections of three point sources provide sufficient information for this calibration. Thereby, it requires only a single measurement of a simple calibration phantom. The calibration is performed immediately after the actual SPECT acquisition by replacing the object in the field of view by the calibration phantom and executing a second SPECT-scan.

Appendix

This appendix derives the equations (16) to (25) by equating the right hand sides of equations (9) and (10) expressed in two different sets of parameters and point source coordinates (11) and (12). Using the cylindrical coordinates, defined by equations (13) to (15), the equations (9) and (10) are first rewritten as

$$u = f\frac{\begin{pmatrix} m\cos\Psi + z\cos\Phi\sin\Psi \\ -\,r\cos(\alpha-\theta)\cos\Psi \\ +\,r\sin(\alpha-\theta)\sin\Phi\sin\Psi \end{pmatrix}}{d + r\cos\Phi\sin(\alpha-\theta) - z\sin\Phi} + m\cos\Psi + e_u, \quad (35)$$

$$v = f\frac{\begin{pmatrix} m\sin\Psi - z\cos\Phi\cos\Psi \\ -\,r\cos(\alpha-\theta)\sin\Psi \\ -\,r\sin(\alpha-\theta)\sin\Phi\cos\Psi \end{pmatrix}}{d + r\cos\Phi\sin(\alpha-\theta) - z\sin\Phi} + m\sin\Psi + e_v, \quad (36)$$

in which the subscript i, indicating the point source number, has been dropped for convenience. Since the point source is assumed to be located off the rotation axis (z-axis) and the detector tilt Φ must lie in the interval $\left]-\frac{\pi}{2},\frac{\pi}{2}\right[$, the coefficient $r\cos\Phi$ in the numerator is nonzero and the above equations can further be rewritten as

$$u = \frac{a_u\cos(\alpha-\theta) + b_u\sin(\alpha-\theta) + c_u}{\sin(\alpha-\theta) + g}, \quad (37)$$

$$v = \frac{a_v\cos(\alpha-\theta) + b_v\sin(\alpha-\theta) + c_v}{\sin(\alpha-\theta) + g}, \quad (38)$$

with

$$a_u = -f\frac{\cos\Psi}{\cos\Phi}, \quad (39)$$

$$a_v = -f\frac{\sin\Psi}{\cos\Phi}, \quad (40)$$

$$b_u = f\frac{\sin\Phi\sin\Psi}{\cos\Phi} + m\cos\Psi + e_u, \quad (41)$$

$$b_v = -f\frac{\sin\Phi\cos\Psi}{\cos\Phi} + m\sin\Psi + e_v, \quad (42)$$

$$c_u = f\left(\frac{m\cos\Psi}{r\cos\Phi} + \frac{z\sin\Psi}{r}\right) + g\,(m\cos\Psi + e_u) \quad (43)$$

$$c_v = f\left(\frac{m\sin\Psi}{r\cos\Phi} + \frac{z\cos\Psi}{r}\right) + g\,(m\sin\Psi + e_v) \quad (44)$$

$$g = \frac{d - z\sin\Phi}{r\cos\Phi}. \quad (45)$$

With the equations (9) and (10) written in this form, the first objective of this calculation is to prove that

$$\widetilde{a}_u = a_u \quad \text{and} \quad \widetilde{a}_v = a_v, \quad (46)$$

$$\widetilde{b}_u = b_u \quad \text{and} \quad \widetilde{b}_v = b_v, \quad (47)$$

$$\widetilde{c}_u = c_u \quad \text{and} \quad \widetilde{c}_v = c_v, \quad (48)$$

$$\widetilde{g} = g, \quad (49)$$

$$\widetilde{\alpha} = \alpha, \quad (50)$$

with $a_u, a_v, b_u, b_v, c_u, c_v, g, \alpha$ and $\widetilde{a}_u, \widetilde{a}_v, \widetilde{b}_u, \widetilde{b}_v, \widetilde{c}_u, \widetilde{c}_v, \widetilde{g}, \widetilde{\alpha}$ being expressed in the different parameter sets (11) and (12). Before proceeding, it should be noticed that the above equations (37) and (38) are only valid for $g > 1$. Geometrically, this restriction simply states that the point source must be located in the field of view for every possible projection angle θ. This remark must be satisfied by any acceptable parameter set, implying that also $\widetilde{g} > 1$.

Equating now the right hand side of equation (37) expressed in the different parameter sets and multiplying with both numerators yields

$$\begin{aligned} &a_u\sin\widetilde{\gamma}\cos\gamma + b_u\sin\widetilde{\gamma}\sin\gamma + (c_u - \widetilde{b_u}g)\sin\widetilde{\gamma} \\ &\quad + a_u\widetilde{g}\cos\gamma + c_u\widetilde{g} = \widetilde{a}_u g\cos\widetilde{\gamma} + \widetilde{c_u}g \\ &+ \widetilde{a}_u\sin\gamma\cos\widetilde{\gamma} + \widetilde{b_u}\sin\gamma\sin\widetilde{\gamma} + (\widetilde{c_u} - b_u\widetilde{g})\sin\gamma, \end{aligned} \quad (51)$$

with

$$\gamma = \alpha - \theta, \quad (52)$$

$$\widetilde{\gamma} = \widetilde{\alpha} - \theta. \quad (53)$$

The products of sines and cosines can further be rewritten, yielding

$$\begin{aligned} &\frac{1}{2}(a_u - \widetilde{a}_u)\sin(\gamma+\widetilde{\gamma}) + \frac{1}{2}(b_u - \widetilde{b_u})\cos(\gamma+\widetilde{\gamma}) \\ &+ (c_u - \widetilde{b_u}g)\sin\widetilde{\gamma} - (\widetilde{c_u} - b_u\widetilde{g})\sin\gamma \\ &+ a_u\widetilde{g}\cos\gamma - \widetilde{a}_u g\cos\widetilde{\gamma} \\ &+ \frac{1}{2}(a_u + \widetilde{a}_u)\sin(\widetilde{\alpha}-\alpha) + \frac{1}{2}(b_u - \widetilde{b_u})\cos(\widetilde{\alpha}-\alpha) \\ &+ c_u\widetilde{g} - \widetilde{c_u}g = 0. \end{aligned} \quad (54)$$

Performing the same operation on equation (38) yields an analogous result, which can be obtained by replacing the subscripts u by v in equation (51) and (54).

The above equation contains a constant part, a part varying with the projection angle θ and a part varying with

2θ. Since the relation must be satisfied for every possible projection angle, these parts may each individually be set equal zero. Doing so for the 2θ-part yields

$$(a_u - \widetilde{a}_u)\sin(\gamma + \widetilde{\gamma}) = (b_u - \widetilde{b_u})\cos(\gamma + \widetilde{\gamma}). \quad (55)$$

Setting the coefficients of the sine and cosine functions equal to zero results in the equations (46) and (47). Setting the other parts of equation (54) now equal to zero, taking into account the above results, yields

$$\begin{aligned}(c_u - b_u g)\sin\widetilde{\gamma} + a_u g\cos\widetilde{\gamma} = \\ (\widetilde{c_u} - b_u\widetilde{g})\sin\gamma + a_u\widetilde{g}\cos\gamma\end{aligned} \quad (56)$$

and

$$a_u\sin(\widetilde{\alpha} - \alpha) + c_u\widetilde{g} - \widetilde{c_u}g = 0. \quad (57)$$

Both the left and right hand side of equation (56) can be written as a cosine with a specific amplitude and phase. Setting the phase of both sides equal to each other yields

$$\widetilde{\alpha} - \alpha = \arctan\left(\frac{\frac{\widetilde{c_u}}{\widetilde{g}} - b_u}{a_u}\right) - \arctan\left(\frac{\frac{c_u}{g} - b_u}{a_u}\right) \quad (58)$$

with $a_u \neq 0$, because $f > 0$ and $\Psi \in \left]-\frac{\pi}{2}, \frac{\pi}{2}\right[$. Further, since $g > 1$, equation (57) can be written as

$$\widetilde{c}_u = c_u\frac{\widetilde{g}}{g} + \frac{a_u}{g}\sin(\widetilde{\alpha} - \alpha). \quad (59)$$

Substituting this relation into equation (58) yields

$$\begin{aligned}\widetilde{\alpha} - \alpha &= \arctan\left(\frac{\frac{c_u}{g} - b_u}{a_u} - \frac{1}{g\widetilde{g}}\sin(\widetilde{\alpha} - \alpha)\right) \\ &\quad - \arctan\left(\frac{\frac{c_u}{g} - b_u}{a_u}\right).\end{aligned} \quad (60)$$

The above equation (60) can be written as

$$H(\beta) = \beta - \arctan(x - y\sin\beta) + \arctan(x) = 0, \quad (61)$$

with

$$\beta = \widetilde{\alpha} - \alpha, \quad (62)$$

$$x = \frac{\frac{c_u}{g} - b_u}{a_u}, \quad (63)$$

$$y = \frac{1}{g\widetilde{g}}. \quad (64)$$

Since the function $H(\beta)$, with $0 < y < 1$, is strictly increasing,

$$\frac{\partial H(\beta)}{\partial\beta} = 1 - \frac{y\cos(\beta)}{1 + (x - y\sin(\beta))^2} > 0, \quad (65)$$

equation (61) has a unique solution $\beta = 0$ or equivalently $\widetilde{\alpha} = \alpha$. Substituting this result back into equation (56) and (57) eventually yields the equations (48) and (49).

The above part derives the equations (46) to (50) for the projection of a point source off the rotation axis. In principle these are already the equations (16) to (25), although in a different form. The remainder of this appendix systematically transforms each of the equations (46) to (50) into the corresponding equations of (16) to (25).

The relations $\widetilde{a}_u = a_u$ and $\widetilde{a}_v = a_v$ yield respectively

$$f\frac{\cos\Psi}{\cos\Phi} = \widetilde{f}\frac{\cos\widetilde{\Psi}}{\cos\widetilde{\Phi}}, \quad (66)$$

$$f\frac{\sin\Psi}{\cos\Phi} = \widetilde{f}\frac{\sin\widetilde{\Psi}}{\cos\widetilde{\Phi}}. \quad (67)$$

Dividing equation (67) by equation (66) leads to equation (16) and substituting this result back into equation (66) or (67) further yields equation (17). The substitution of the equations (16) and (17) into the relations $\widetilde{b}_u = b_u$ and $\widetilde{b}_v = b_v$ immediately yields the equations (22) and (23). The equations $\widetilde{c}_u = c_u$ and $\widetilde{c}_v = c_v$ yield respectively

$$\begin{aligned}\frac{fm}{r\cos\Phi}\cos\Psi + \frac{fz}{r}\sin\Psi + g(m\cos\Psi + e_u) = \\ \frac{f\widetilde{m}}{\widetilde{r}\cos\Phi}\cos\Psi + \frac{\widetilde{f}\widetilde{z}}{\widetilde{r}}\sin\Psi + g(\widetilde{m}\cos\Psi + \widetilde{e_u})\end{aligned} \quad (68)$$

and

$$\begin{aligned}\frac{fm}{r\cos\Phi}\sin\Psi - \frac{fz}{r}\cos\Psi + g(m\sin\Psi + e_v) = \\ \frac{f\widetilde{m}}{\widetilde{r}\cos\Phi}\sin\Psi - \frac{\widetilde{f}\widetilde{z}}{\widetilde{r}}\cos\Psi + g(\widetilde{m}\sin\Psi + \widetilde{e_v}),\end{aligned} \quad (69)$$

in which $\widetilde{g} = g$ and equation (17) have already been used. Further, with equations (22) and (23), $(\widetilde{m}\cos\Psi + \widetilde{e_u})$ and $(\widetilde{m}\sin\Psi + \widetilde{e_v})$ can be written in function of $(m\cos\Psi + e_u)$ and $(m\sin\Psi + e_v)$ respectively, yielding

$$\begin{aligned}\frac{f\widetilde{m}}{\widetilde{r}\cos\Phi}\cos\Psi + \frac{f\widetilde{z}}{\widetilde{r}}\sin\Psi + g\left(\frac{f(\sin\Phi - \sin\widetilde{\Phi})}{\cos\Phi}\right)\sin\Psi \\ = \frac{fm}{r\cos\Phi}\cos\Psi + \frac{fz}{r}\sin\Psi\end{aligned} \quad (70)$$

and

$$\begin{aligned}\frac{f\widetilde{m}}{\widetilde{r}\cos\Phi}\sin\Psi - \frac{f\widetilde{z}}{\widetilde{r}}\cos\Psi - g\left(\frac{f(\sin\Phi - \sin\widetilde{\Phi})}{\cos\Phi}\right)\cos\Psi \\ = \frac{fm}{r\cos\Phi}\sin\Psi - \frac{fz}{r}\cos\Psi.\end{aligned} \quad (71)$$

Multiplying equation (70) and (71) by $\cos\Psi$ and $\sin\Psi$ respectively, adding the results and using equation (17) eventually yields equation (21). The substitution of equation (21) and (17) into equation (70) or (71) further yields equation (19), (24) and (25). Using this result to substitute the term $\frac{\widetilde{z}}{\widetilde{r}}$ in $\widetilde{g} = g$ finally yields equation (20).

References

[1] A. Seret, M. Defrise, and D. Blocklet, "180 degree pinhole SPECT with tilted detector and OSEM reconstruction: phantom studies and potential clinical applications," *Eur. J. Nucl. Med.*, vol. 28, pp. 1836–1841, 2001.

[2] A. Spanu, G. Dettori, F. Chessa, A. Porcu, P. Cottu, P. Solinas, A. Falchi, M. E. Solinas, A. M. Scanu, S. Nuvoli, and G. Madeddu, "99mTc-Tetrofosmin pinhole-SPECT (P-SPECT) and radioguided sentinel node (SN) biopsy and in breast cancer axillary lymph node staging," *Cancer Biother. Radiopharm.*, vol 16(6), pp. 501–513, 2001.

[3] Y. W. Bahk, S. K. Chung, Y. H. Park, S. H. Kim, and H. K. Lee, "Pinhole SPECT imaging in normal and morbid ankles," *J. Nucl. Med.*, vol. 39, pp. 130–139, 1998.

[4] M. F. Smith, D. R. Gilland, R. E. Coleman, and R. J. Jaszczak, "Quantitative Imaging of Iodine-131 Distributions in Brain Tumors with Pinhole SPECT: A Phantom Study," *J. Nucl. Med.*, vol. 39(5), 1998.

[5] P. M. Wanet, A. Sand, and J. Abramovici, "Physical and Clinical Evaluation of High-Resolution Thyroid Pinhole Tomography," *J. Nucl. Med.*, vol. 37, pp. 2017–2020, 1996.

[6] D. A. Weber, and M. Ivanovic, "Ultra-high resolution imaging of small animals: implementations for preclinical and research studies," *J. Nucl. Cardiol.*, vol. 6(3), 1999.

[7] P. D. Acton, S. Choi, K. Plössl, and H. F. Kung, "Quantification of dopamine transporters in the mouse brain using ultra-high resolution single-photon emission tomography," *Eur. J. Nucl. Med.*, vol. 29, pp. 691–698, 2002.

[8] D. P. McElroy, L. R. MacDonald, F. J. Beekman, Y. Wang, B. E. Patt, J. S. Iwanczyk, B. M. W. Tsui, and E. J. Hoffman, "Evaluation of A-SPECT: A Desktop Pinhole SPECT System for Small Animal Imaging," in *Proc. IEEE Nuclear Science Symposium*, 2001, M10-4.

[9] J. B. A. Habraken, K. de Bruin, M. Shehata, J. Booij, R. Bennink, B. L. F. van Eck Smit, and E. B. Sokole, "Evaluation of High-Resolution Pinhole SPECT Using a Small Rotating Animal," *J. Nucl. Med.*, vol. 42, pp. 1863–1869, 2001.

[10] L. R. MacDonald, B. E. Patt, J. S. Iwanczyk, B. M. W. Tsui, Y. Wang, E. C. Frey, D. E. Wessel, P. D. Acton, and H. F. Kung, "Pinhole SPECT of Mice Using the LumaGEM Gamma Camera," *IEEE Trans. Nucl. Sci.*, vol. NS-48(3), pp.830–836, 2001.

[11] M. C. Wu, H. R. Tang, D. W. Gao, A. Ido, J. W. O'Connell, B. H. Hasegawa, and M. W. Dae, "ECG-Gated Pinhole SPECT in Mice with Millimeter Spatial Resolution," *IEEE Trans. Nucl. Sci.*, vol. NS-47(3), 2000.

[12] T. Hirai, R. Nohara, R. Hosokawa, M. Tanaka, H. Inada, Y. Fukibayashi, M. Fujita, J. Konishi, and S. Sasayama, "Evaluation of myocardial infarct size in rat heart by pinhole SPECT," *J. Nucl. Cardiol.*, vol. 7(2), 2000.

[13] M. C. Wu, H. R. Tang, J. W. O'Connell, D. W. Gao, A. Ido, A. J. Da Silva, K. Iwata, B. H. Hasegawa, and M. W. Dae, "An Ultra High Resolution ECG-Gated Myocardial Imaging System for Small Animals," *IEEE Trans. Nucl. Sci.*, vol. NS-46(4), 1999.

[14] K. Ogawa, T. Kawade, K. Nakamura, A. Kubo, and T. Ichihara, "Ultra high resolution pinhole SPECT for small animal study," *IEEE Trans. Nucl. Sci.*, vol. NS-45(6), pp. 3122–3126, 1998.

[15] G. T. Gullberg, B. M. W. Tsui, C. R. Crawford, J. G. Ballard, and J. T. Hagius, "Estimation of geometrical parameters and collimator evaluation for cone beam tomography," *Med. Phys.*, vol. 17(2), pp. 264–272, 1990.

[16] J. Li, R. J. Jaszczak, H. Wang, K. L. Greer and, R. E. Coleman, "Determination of both mechanical and electronic shifts in cone beam SPECT," *Phys. Med. Biol.*, vol. 39, pp. 743–754, 1993.

[17] H. Wang, M. F. Smith, C. D. Stone, and R. J. Jaszczak, "Astigmatic single photon emission computed tomography imaging with a displaced center of rotation," *Med. Phys.*, vol. 25(8), pp. 1493–1501, 1998.

[18] Ph. Rizo, P. Grangeat, and R. Guillemaud, "Geometric Calibration Method for Multiple-Head Cone-Beam SPECT System," *IEEE Trans. Nucl. Sci.*, vol. NS-41(6), pp. 2748–2757, 1994.

[19] K. J. Kyriakopoulos, P. Yiannakos, V. Kallipolites, and K. Domales, "A Geometric Calibration Methodology for Single-Head Cone-Beam X-Ray Systems," *Journal of Intelligent and Robotic Systems*, vol. 24, pp. 151–174, 1999.

[20] A. V. Bronnikov, "Virtual alignment of x-ray cone-beam tomography system using two calibration aperture measurements," *Opt. Eng.*, vol. 38(2), pp. 381–386, 1999.

[21] F. Noo, R. Clackdoyle, C. Mennessier, T. A. White, and T. J. Roney, "Analytic method based on identification of ellipse parameters for scanner calibration in cone-beam tomography," *Phys. Med. Biol.*, vol. 45, pp. 3489–3508, 2000.

[22] F. Noo, C. Mennessier, R. Clackdoyle, T. A. White, and T. J. Roney, "Non-iterative methods for scanner calibration in cone-beam tomography," in *Proc. International Meeting on Fully Three-Dimensional Image Reconstruction in Radiology and Nuclear Medicine*, 1999, pp. 155–158.

[23] W. H. Press, *Numerical recipes : the art of scientific computing.* Cambridge: Cambridge University Press, 1986, pp.294–301.

[24] H. M. Hudson, and R. S. Larkin, "Accelerated Image Reconstruction Using Orderes Subsets of Projection Data," *IEEE Trans. Med. Imag.*, vol. MI-13(4), pp. 601–609, 1994.

[25] C. Vanhove, M. Defrise, P. R. Franken, H. Everaert, F. Deconinck, and A. Bossuyt, "Interest of ordered subsets expectation maximization (OS-EM) algorithm in pinhole single-photon emission tomography reconstruction: a phantom study," *Eur. J. Nucl. Med.*, vol. 27(2), pp. 140–146, 2000.

[26] L. A. Shepp, and Y. Vardi, "Maximum Likelihood Reconstruction for Emission Tomography," *IEEE Trans. Med. Imag.*, vol. MI-1(2), pp. 113–122, 1982.

[27] M. F. Smith, and R. J. Jaszczak, "The effect of gamma ray penetration on angle-dependent sensitivity of pinhole collimation in nuclear medicine," *Med. Phys.*, vol. 24(11), pp. 1701–1709, 1997.